Applied Thermal Engineering 130 (2018) 710–721

Contents lists available at ScienceDirect

Applied Thermal Engineering

journal homepage: www.elsevier.com/locate/apthermeng

Research Paper

Enhancing thermal stability and uniformity in boiling heat transfer using micro-nano hybrid surfaces (MNHS)

Donghwi Lee [a,1], Namkyu Lee [a,1], Dong Il Shim [a], Beom Seok Kim [b], Hyung Hee Cho [a,*]

[a] Department of Mechanical Engineering, Yonsei University, 50 Yonsei-ro, Seodaemun-gu, Seoul 120-749, Republic of Korea
[b] DEMO Technology Division, National Fusion Research Institute (NFRI), 169-148 Gwahak-ro Yuseong-gu, Daejeon 34133, Republic of Korea

HIGHLIGHTS

- Pool boiling experiment is conducted on micro-nano hybrid surfaces (MNHS).
- Thermal stability is evaluated using a local temperature-measuring sensor of RTD.
- CHF and thermal stability are analyzed by the bubble merger phenomena on MNHS.
- MNHS notably enhance CHF by delaying bubble merger and maximizing bubble density.
- MNHS reduce spatial/temporal temperature variation at CHF to less than 1/3 and 1/4.

ARTICLE INFO

Article history:
Received 23 February 2017
Revised 27 September 2017
Accepted 27 October 2017
Available online 13 November 2017

Keywords:
Boiling heat transfer
Micro-nano hybrid surface
Thermal uniformity and stability
Critical heat flux
Bubble coalescence

ABSTRACT

In two-phase heat transfer, promising issues include not only improving the boiling performance but also the surface temperature uniformity and stability, which indicate that how long the system maintains thermal stability without a failure on the surface. In this study, the merits of micro-nano hybrid surfaces (MNHS) are discussed for enhancing the thermal uniformity/stability and boiling heat transfer performance. Spatial/temporal heat transfer characteristics are evaluated on MNHS using a local temperature-measuring sensor of resistance temperature detector (RTD). We demonstrate that MNHS can enhance not only boiling performance but also thermal uniformity/stability by delaying bubble coalescence with an appropriate design of the location of the nucleation sites and the nucleated bubble size. The confining effects of nucleated bubbles on nanowire (NW) structures and of uniform bubble nucleation on uniformly distributed micro-cavity (MC) structures lead to the reliable enhancement of thermal uniformity/stability as well as critical heat flux (CHF) in pool boiling environments. These combined effects of the NW and MC structures could delay the bubble coalescence phenomenon by catalyzing bubble nucleation dispersedly and quickly at small bubble sizes. When the normalized pitch of the nucleation sites is 1, namely the pitch of the nucleation sites and the bubble departure size have the same dimension, CHF is significantly enhanced, by more than 170%, on an MNHS versus a plain surface by delaying bubble coalescence and maximizing bubble density. Boiling heat transfer using an MNHS represents a breakthrough reducing the spatial and temporal temperature variation at CHF to less than 1/3 and 1/4, respectively, compared with a plain surface.

1. Introduction

In accordance with advances in technology, huge and repeated locally concentrated thermal loads are generated due to high temperature gradients in devices such as electrical device, nuclear reactors, gas turbines, and nuclear fusion devices [1,2]. Such locally concentrated thermal loads will ultimately cause thermal stress and fatigue, which are major reasons for the fatal failure of surfaces. Thus, effective cooling technologies ensuring thermal uniformity/stability should be used to cool such devices, releasing the concentrated thermal load. One such potential cooling technology is boiling heat transfer, which is based on a phase-change phenomenon that entails heterogeneous nucleation of a liquid coolant for extremely high heat-dissipating applications [3].

One of the most important performance factors in boiling heat transfer is the critical heat flux (CHF). The CHF is defined by the

* Corresponding author.
E-mail address: hhcho@yonsei.ac.kr (H.H. Cho).
[1] These authors contributed equally to this work.

https://doi.org/10.1016/j.applthermaleng.2017.10.144
1359-4311/

Nomenclature

A	area (m^2)
D	diameter (m)
I	current (A)
k	thermal conductivity (W/m·K)
P	perimeter (m)
q	heat flux (W/m^2)
R	radius (m)
r	roughness
s	pitch of nucleation sites (m)
T	temperature (°C)
t	thickness (m)
V	voltage (V)
w	width (m)
x	bubble merged diameter (m)
y	number of bubbles

Greek letters

Δ	difference
δ	thickness of thermal boundary layer
θ	contact angle (°)
ρ	density (kg/m^3)
σ	standard deviation

Subscripts

avg	average
b	bubble
c	center
cv	curve
e	equivalent
eff	effective
h	heater
o	offset
r	resistance temperature detector (RTD)
Si	silicon
sat	saturated
sub	subcooled
t	thickness
v	vapor
w	wall

Superscript

$*$	ideal condition

upper limit of the heat flux resulted from intermittently dry-out of the heating surfaces and following abrupt wall temperature increases within the slug and columns region where the vigorous bubble coalescences occur [4,5]. Thus, there have been many studies on enhancing CHF by delaying bubble coalescence using various techniques, such as surface morphology and wettability control [6,7]. Microstructures, such as pillars and cavities, can be effective in delaying bubble coalescence by causing discrete bubble nucleation [8–11]. Especially, micro-cavity (MC) structures have the advantage of controlling the location of bubble nucleation sites precisely [12–15]. However, MC structures have a disadvantage in supplying coolant to the heating surface in comparison with nanoscale structures. Because MC structures have limitation to increase surface wettability compared to nanoscale structures which have superhydrophilic characteristics. Therefore, in recent years, many studies have been conducted on CHF enhancement using nanoscale structures, such as nanowires [16–20]. In particular, Nanowire (NW) structures significantly enhance the CHF, not only due to their superhydrophilic characteristics, but also by generating dispersed, small, and high frequency bubbles, which enable a liquid path to be secured for direct contact with the boiling surface and working fluid, by means of 1–2 μm natively formed micro-cavities [21–23]. However, in contrast to artificial MC structures, because random natively formed micro-cavities are inevitably produced during the NW fabrication process, it is hard to control the location of bubble nucleation sites precisely on NW structures.

In previous research, there have been many efforts to enhance boiling performance using micro-nanowire hybrid surfaces (MNHS) by increase of surface wettability (contact angle (CA), wicking) [24–29]. However, there has been relatively little research on enhancing boiling performance using MNHS by preventing bubble coalescence using artificial control of bubble dynamics, such as the location of bubble nucleation sites and nucleated bubble size [30].

In this study, we fabricated an MNHS to enhance the boiling performance and thermal stability/uniformity, by delaying bubble coalescence using control of the location of nucleation sites and nucleated bubble size. The MNHS was fabricated by a two-step silicon etching process, which involved etching for micro patterning and metal-assisted chemical etching (MaCE) for NW synthesis [31]. The MNHS fabrication method is simple and precise, and can readily produce an MNHS over the area of an entire wafer. Pool boiling experiments were conducted under saturated temperature at atmosphere pressure conditions on plain, MC, and NW surfaces, and the MNHS. We demonstrate that the MNHS was able to enhance not only CHF, but also thermal stability/uniformity by delaying bubble coalescence and maximizing bubble density with appropriate design of the location of nucleation sites and control of nucleated bubble size.

2. Experimental apparatus

2.1. Preparation of micro-nanowire hybrid surfaces (MNHS)

To fabricate MNHS, we used a two-step silicon etching process, composed of deep trench reactive ion etching (DRIE) and wet etching (electroless etching). MNHS with MC and NW structure is schematically shown in Fig. 1(a). First, microstructures were fabricated by dry etching using a P-type silicon wafer (resistivity 1 to 20 Ω cm doped with boron). In the silicon dry process (Bosch process), which is widely used as a dry etching method for making deep silicon trenches, a passivation layer (polymeric C_4F_8) was deposited to prevent over-etching of the sidewalls of the silicon trenches. This layer can be left in place or removed from the sidewalls of the microstructure by selecting the appropriate PR striping method. To fabricate microstructures without a thin sidewall structure, the PR and polymeric passivation layers deposited on the sidewalls should be removed by the Asher process. The fabricated microstructure is shown in Fig. 1(b).

The NW surface was fabricated using a MaCE method [32]. We cleaned the substrate using a Piranha solution (3:1 mix of H_2SO_4: H_2O_2) and immersed the selectively exposed sensor, with a Teflon case, in the solution for 40 min. Further, the substrate was washed with methanol and acetone for 5 min, respectively. Next, the exposed area of the sensor, the opposite side to the RTD and ITO circuits on the sensor was exposed to an etching solution (a mix of 5 M HF and 0.02 M $AgNO_3$) at room temperature. The Ag + ions contained in the solution are naturally attached to the exposed silicon surface through an electrolytic substitution reaction. Oxidation takes place at the point of contact between the silicon

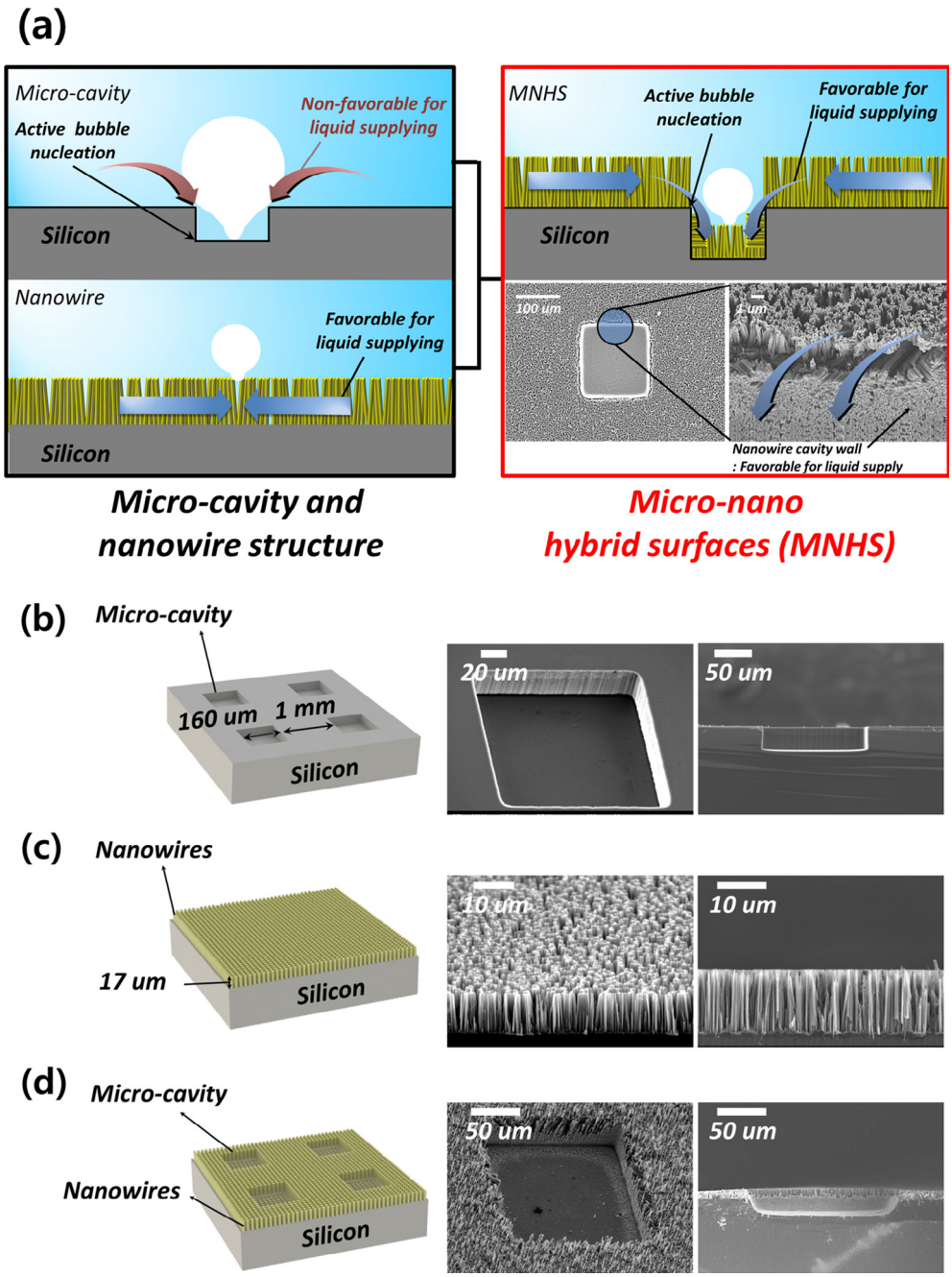

Fig. 1. Schematics and scanning electron microscopy (SEM) images of micro-cavity, nanowire and micro-nanowire hybrid surfaces (MNHS). (a) Schematics of different liquid supplying and bubble formation for various surfaces. Dimensions and SEM images of (b) micro-cavity, (c) nanowire and (d) MNHS.

surface and the Ag + ions and is followed by an immediate etch reaction by HF. Therefore, the vertically aligned NW structure can be formed from the remaining un-etched silicon portions. In this study, an NW surface (average height 17 μm) was fabricated as shown in Fig. 1(c). The Fabricated NWs on silicon substrates contains naturally formed microscale cavities (up to 1–2 μm in size) formed by van der Waals forces between the nanowires. Finally, MNHS with MC and NW structures was fabricated by combining these two structures as shown in Fig. 1(d).

2.2. Characterization of morphology and contact angle

MNHS was characterized by field emission-scanning electron microscopy (FE-SEM) (JEOL-JSM-7001F, JEOL Ltd., Japan). The average height and pitch of MNHS were measured using FE-SEM images. Microscope I'Measure software (Ingplus, Korea) was used to determine the average diameter of the natural microscale cavities of the NW structure and the diameter of the artificial micro cavities of the MC structures. This software analyzes the equivalent diameter of natural microscale cavities on the NW structures and the diameter of artificial microscale cavities on the MC structure. This is based on the assumption that the shape of the microscale cavity is a perfect circle. The data measured for five frames with high resolution (×2500) SEM images were averaged to determine the equivalent diameters of the natural microscale cavities and artificial micro cavities on the NW and MC surfaces, respectively. Apparent CAs on plain, MC, and NW surfaces, and MNHS were characterized using a contact angle measurement system (KSV

CAM-200; KSV Instruments, Finland). The images were acquired using a high-speed camera with a resolution of 512 × 480 pixels and a time interval of 2 ms. CAs were measured based on the images captured when water droplets contacted the solid surfaces. The volume of water droplets was 2 μL, and the CA was determined by averaging the five measured values under the same conditions.

2.3. Visualization and analysis of bubble characteristics

Using a high-speed camera (Speedsense M310, Dantec, Denmark) and bubble visualization imaging software (version 3.30, Dynamic Studio, Denmark), we obtained an images of the departing bubbles by providing backlight with an 80 W LED. Bubble departure characteristics were visualized using the shadowgraph method on the plain, MC, and NW surfaces, and on MNHS at the onset of nucleate boiling (ONB) and at the partial nucleate boiling region. Detailed bubble departure behavior video clip is contained in Supplementary Movie 1.

The bubble-merged diameters were analyzed with the bubble visualization imaging software, using the particle characteristic analysis function. The software analyzes the equivalent merged diameters of bubbles by assuming that the recorded 2D image of the merged bubble is a perfect circle. The equation for the equivalent merged diameter is as follows:

$$d_e = 1.55 \cdot \frac{A_b^{0.625}}{P_b^{0.25}} \quad (1)$$

where A_b and P_b are the cross-sectional area and perimeter of the bubble, respectively [33]. The detail bubble-merged behavior video clip is contained in Supplementary Movie 2.

2.4. Pool boiling experimental condition

Fig. 2(a) is a schematic diagram of an experimental pool boiling apparatus, composed of a reservoir, a test section, a data acquisition system, and a bubble-visualization system. The bulk temperature of the working fluid in the main reservoir was controlled by two immersion type heaters and a coil type heat exchanger. The working fluid temperature was controlled by a proportional integral differential (PID) temperature controller of the immersion heater and the heat exchanger connected to a constant temperature water bath. Two K-shaped thermocouples were installed at different heights of the reservoir to measure the local temperature of the fluid and to confirm the steady state. A pressure gauges and vapor exhaust valves are installed to monitor pressure conditions and maintain the atmospheric pressure in the boiling chamber, respectively. Transparent windows on the side of the reservoir allowed bubbles to be visualized. The test section, for installing a local temperature measurement sensor is located in the center of the reservoir. The body and bottom of the test specimen were made of Macerite ceramics (melting point of 1200 °C and thermal conductivity of 1.6 W/m·K) and polyether ether ketone (PEEK; thermal conductivity of 1.7 W/m·K), respectively, to reduce conductive heat loss and avoid failures, even at CHF. Data acquisition system was connected to the sensor for signal acquisition and current supply can be achieved by using a power supply, respectively. Electrical connections were made through spring probes and copper rods with electrodes of the sensor. The power supply was used to control the current through the ITO heater on the sensor and adjust heat flux values during boiling experiment. Data acquisition system analyzes electrical signals such as the electrical resistance of the RTD sensor, temperature of the reservoir, and the current and voltage drop of the ITO heater. In this study, deionized water was used as the working fluid and preliminary degassing was performed for 2 h before the experiment. We performed pool boiling heat transfer experiments at saturated temperatures under ambient pressure conditions. All experiments were performed under steady state conditions for the bulk fluid temperature and heat flux of the ITO heater. To achieve constant heat flux conditions, the voltage drop and RTD signals were monitored for more than 3 min at each measurement after current adjustment. The surface temperature data from the RTD sensor were collected at 1000 Hz and the voltage drop and thermocouple signals were measured at 2 Hz. Data presented here are averaged values from 30 s measurements obtained under steady state conditions.

2.5. Local temperature-measuring sensor

A sensor chip composed of a thin film heater (indium-tin-oxide [ITO], 500 nm thick) and four-wire platinum resistance temperature detectors (RTD) with five measurement points (1–5) was designed for local temperature characterization. Fig. 2(b) shows the fabricated local temperature sensor. The distance between the measurement points is 1.5 mm and the ITO heater with a heating area of 0.5 × 1.0 cm^2, is at the center of the sensor chip (7.5 × 2.5 cm^2). This sensor chip provides high accuracy and

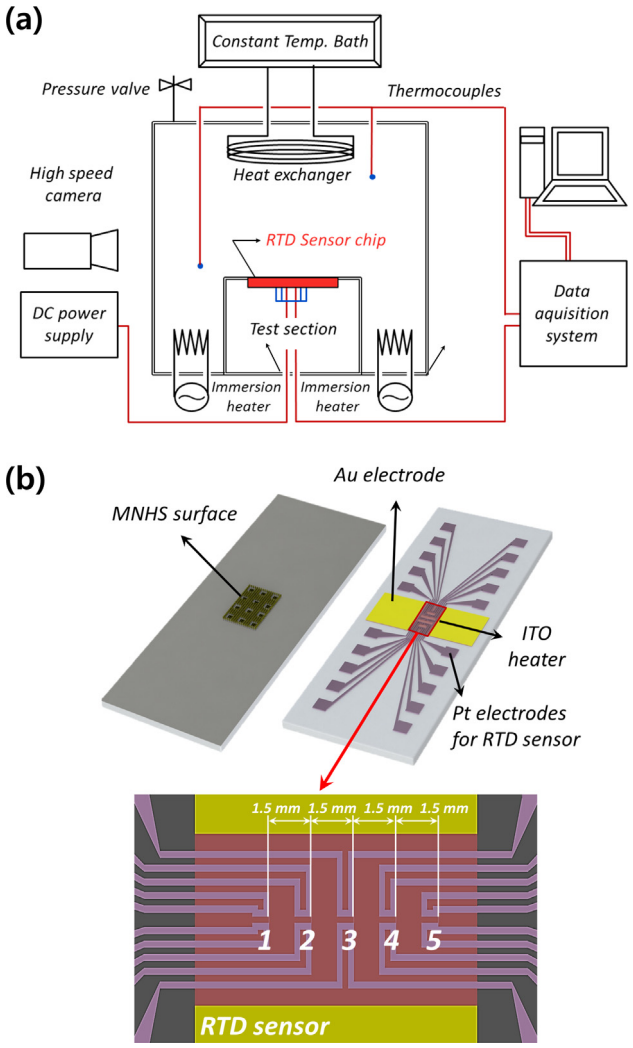

Fig. 2. Schematic diagram of the pool-boiling system and local temperature-measuring sensor. (a) Pool-boiling experimental apparatus. (b) Integrated heater and resistance temperature detector (RTD) sensor (top) and locations of five RTD sensors (bottom).

reliability in terms of surface temperature measurement through the RTD of the boiling surface, thus reducing any perturbation caused by the installation process. The response time of the sensor was 2.84 ms and was designed to be faster than the bubble departure frequency of tens to hundreds of Hertz. Details of the fabrication of the sensor chip can be found in previous papers [34].

2.6. Data reduction

The applied heat flux, q'', is estimated by the applied induced I, voltage drop from the heater, V, and limited heating area, A, and can be expressed as $q'' = V \cdot I/A$. The RTD sensor and ITO heater are located on the bottom surface of the test specimen. Because the silicon substrate has thin thickness (500 μm) and high thermal conductivity (140 W/m·K), we consider that one-dimensional conduction heat transfer according to Fourier's law is reasonable to predict T_w from T_r [34]. Therefore, the exact boiling surface temperature can be achieved as $T_w = T_r - (q'' \cdot t_{Si})/k_{Si}$ taking into account 1-D conduction, where T_w, T_r, t_{Si}, and k_{Si} are the wall temperature on the boiling surface, temperature measured from RTD, thickness of the silicon wafer, and thermal conductivity of the silicon wafer, respectively. For the unique markers of heat flux during boiling, ONB is determined by first bubble observation, and CHF is evaluated by detecting temporal surface temperature fluctuations above 15 K. Because we were concerned that CHF may damage the experimental apparatus, we predicted CHF as described, and the quantitative value was calculated by adding half of the increment between the last heat flux showing the vigorous fluctuation and the previous one, before observing the warning signal.

2.7. Uncertainty analysis

All errors related to the experiments presented in this study were estimated with 95% confidence level, using measured data for each variable. The uncertainty analysis was performed on the main variables described in the above data reduction procedure as well as the basic dimension variables, and was based on Moffat's method [35]. Errors for dimensional estimations in terms of the fabrication of the RTD sensor, and for temperature measurement by thermocouples, were ±0.2% and ±0.05%, respectively. For the uncertainty in heat flux, it is difficult to calculate the amounts of dissipated heat flux by pure boiling phenomena towards the external environment due to the complex boundary conditions. Therefore, the major heat loss that could cause the uncertainty was estimated by a numerical 3D analysis using a commercial CFD code, Fluent 6.3.26 (ANSYS), and validating its results with experimental ones. Using the measured temperature at the center point of the RTD, we extracted representative temperature values for comparison. However, since the boiling heat transfer coefficient cannot be directly measured, initial boundary conditions were first adopted from the experimental data and iterative calculations with the previously developed boundary calculations were performed. At certain heat-flux values, the surface temperatures were monitored until we obtained a deviation below 1% from the experimental temperature value. At the satisfied condition, heat flux towards the external environment on the heater surface was compared to the input heat-flux condition, and we estimated the quantitative heat loss. In regard to this heat-loss prediction, the uncertainty in the applied heat flux was compensated as $(\delta q''/q'') = [(\delta V/V)^2 + (\delta I/I)^2 + (\delta A_h/A_h)^2]^{1/2} + q''_{loss}$, and was 6.5%. The uncertainties for the wall temperature and convective heat transfer coefficient were analyzed according to the same procedure used for the uncertainty calculation; they were 6.5% and 9.2%, respectively. In terms of bubble shadow images obtained from the visualization, the pixel uncertainty in the bubble diameter was ±0.1 mm.

3. Results and discussions

3.1. Boiling performance and nucleation characteristics

The critical heat flux (CHF) of boiling heat transfer is related to bubble coalescence and wicking phenomena [36,37]. MC structures are able to generate bubbles selectively by locally concentrated heat flow, using arranged micro cavities that affect the delay in bubble coalescence. NW structures can not only supply liquid to the surface by hemi-wicking phenomena, but also decrease the bubble diameter at the nucleation site due to the natively formed micro cavity morphology. For these reasons, as shown in Fig. 1(a), we fabricated a micron MNHS to enhance CHF, taking advantage of MC and NW structures. Fig. 1(b) shows the dimensions of the MC: 160 μm diameter, 30 μm depth, and 1 mm pitch between adjacent cavities. Fig. 1(c) shows the dimensions of the NW structures, 17 μm high, and Fig. 1(d) shows the MNHS dimensions, which are the same as those of the MC and NW structures. In this study, pool boiling experiments were conducted to evaluate the boiling heat transfer performance of MNHS under saturated conditions.

Fig. 3 shows the boiling heat transfer characteristics with wall superheat. In Fig. 3, the blue arrows indicate ONB, which is the starting point of boiling heat transfer, and the black arrows indicate CHF, which is the maximum heat dissipation capacity of the surface. The results show that MNHS has increased boiling performance, in terms of both ONB and CHF. For ONB, MNHS reduced the wall superheat for the starting point of the phase change by 15.8 K, 6.8 K, and 3.1 K, in comparison with the plain, MC, and NW surfaces, and the CHF of the MNHS was enhanced, by 172%, 118%, and 23%, versus the plain, MC, and NW surfaces, respectively. We thought that the micro and nanostructures should each have a role in the boiling heat transfer enhancement of the MNHS. Thus, to explain the results of CHF enhancement, we analyzed the phenomena related to the micro and nanostructures with regard to boiling heat transfer. First, we analyzed the ONB results for MC and NW. Regarding the plain and MC surfaces, MC has a faster ONB than the plain surface. As shown in Fig. 4(a), because heat flow concentrates towards the tip of the MC and causes a higher temperature than in the remaining surface, bubble nucleation at the cavity occurs faster than on a plain surface [38]. In Fig. 4(a), bubble ebullition occurs at the MC. This means that the MC has a role in indicating the nucleate site for bubble nucleation. Regarding the NW surface, it has a faster ONB than the MC and plain surfaces. Fig. 4(b) shows bubble nucleation characteristics at ONB on plain, MC, and NW surfaces, and on the MNHS. To explain the faster ONB on the NW surface, we calculated the effective nucleation site, based on Hsu's theory [39], as follows:

$$\left\{ \begin{matrix} r_{eff,min}(\Delta T_w, \Delta T_{sub}) \\ r_{eff,max}(\Delta T_w, \Delta T_{sub}) \end{matrix} \right\} = \frac{\delta_t D_2}{2D_1} \cdot \frac{\Delta T_w}{\Delta T_w + \Delta T_{sub}} \times \left[1 \left\{ \begin{matrix} - \\ + \end{matrix} \right\} \sqrt{1 - \frac{8 D_1 \gamma T_{sat}(P_l)(\Delta T_w + \Delta T_{sub})}{\rho_v l \delta_t (\Delta T_w)^2}} \right], \quad (2)$$

where ΔT_w, ΔT_{sub}, δ_t, T_{sat}, ρ_v, and l are the wall superheat, degree of subcooling, thermal boundary layer thickness, liquid saturation temperature, density of fluid, and latent heat of fluid, respectively. As shown in Fig. 4(c), from Hsu's theory, the NW has a lower range of effective nucleate site radii at the same wall superheat. The NW surface has numerous cavities, of 1–2 μm, which are effective nucleation sites at low superheat and can work in boiling heat transfer. MC also has cavities for the concentration of heat flow and helps bubble nucleation compared with a plain surface, but it is not suitable for activating effective nucleation sites in boiling heat transfer,

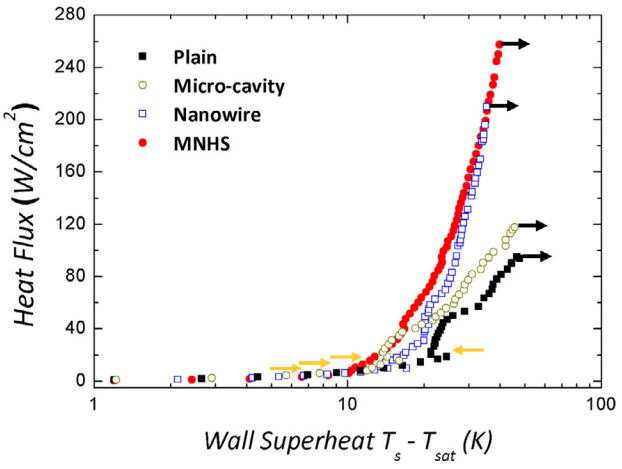

Fig. 3. Boiling curves on various surfaces; plain, micro-cavity, nanowire and MNHS. Black arrows indicate CHF and yellow arrows indicate the onset of nucleate boiling (ONB). (For interpretation of the references to color in this figure legend, the reader is referred to the web version of this article.)

according to Hsu's theory. Thus, the reason why ONB occurs more rapidly on the MNHS surface is a combination of the increase in local temperature caused by MC and the numerous effective cavities for bubble ebullition, due to the NW surface.

Based on these results, we analyzed the CHF of the MNHS, based on the results of the MC and NW surfaces. CHF is related to the surface wettability, expressed by the CA, and bubble dynamics, consisting of the bubble diameter and frequency. Fig. 5(a) shows apparent contact angles on various surfaces; plain, MC, NW and MNHS. Fig. 5(b) shows the CHF distribution with surface CA, based on Kandlikar's correlation [40]. As shown in Fig. 5(a), the CA between plain ($\theta = 46.5°$) and MC ($\theta = 47.2°$) is similar, but the CHF is 24% different between the surface. This suggests that the bubble dynamics on the plain and MC surfaces would differ and be important in explaining the CHF enhancement. In Fig. 5 (c) and (d), the graph shows that bubble characteristics at each surface, represented by bubble departure diameter and frequency with heat flux, increase for a single bubble. It also shows that bubble departure diameter decreases, and bubble departure frequency increases slightly, on the MC surface versus the plain surface,

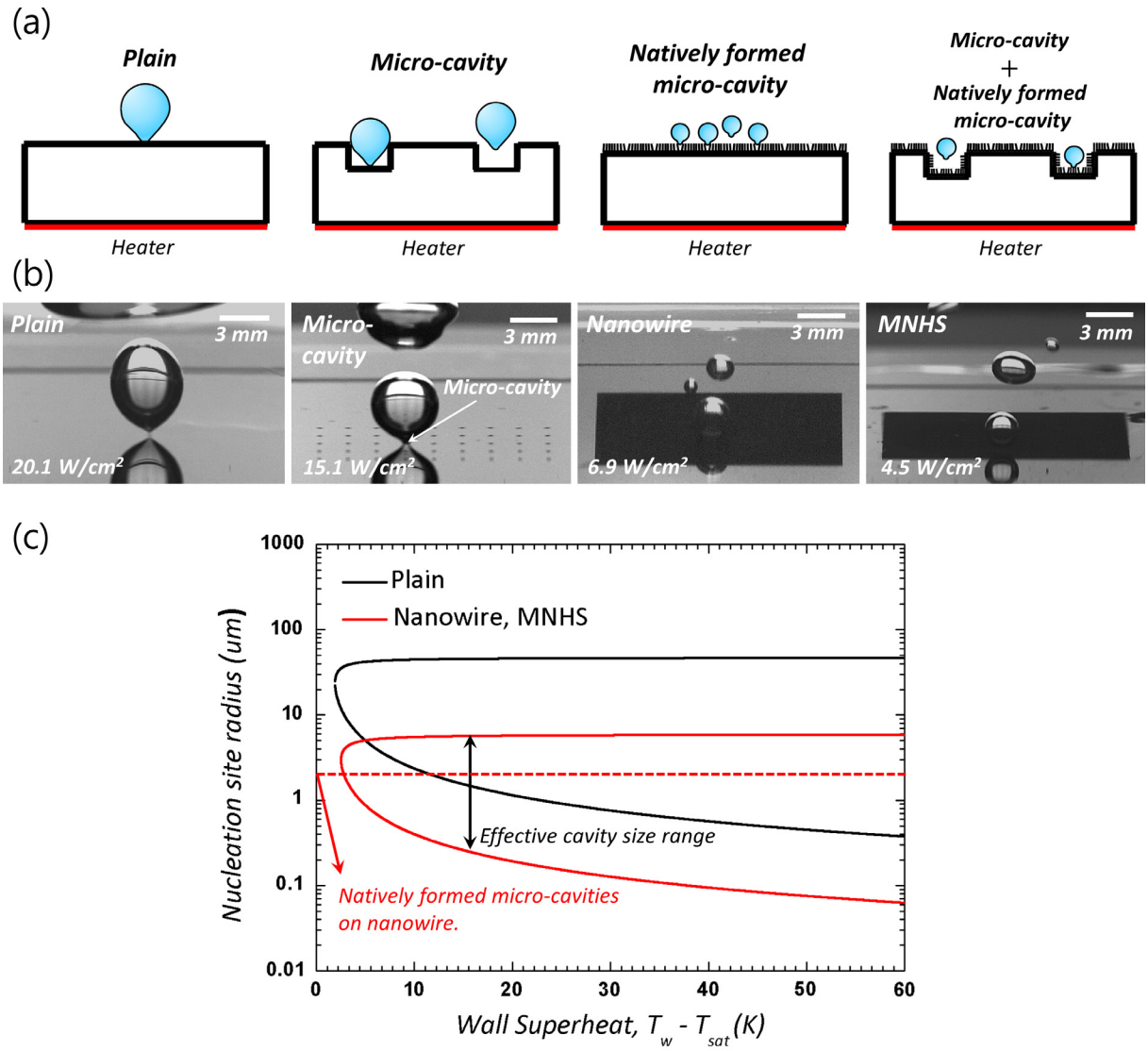

Fig. 4. Bubble nucleation characteristics on various surfaces; plain, micro-cavity, nanowire and MNHS. (a) Schematics of bubble nucleation. (b) Photographs for the bubble nucleation. (c) Effective cavity radius of bubble nucleation.

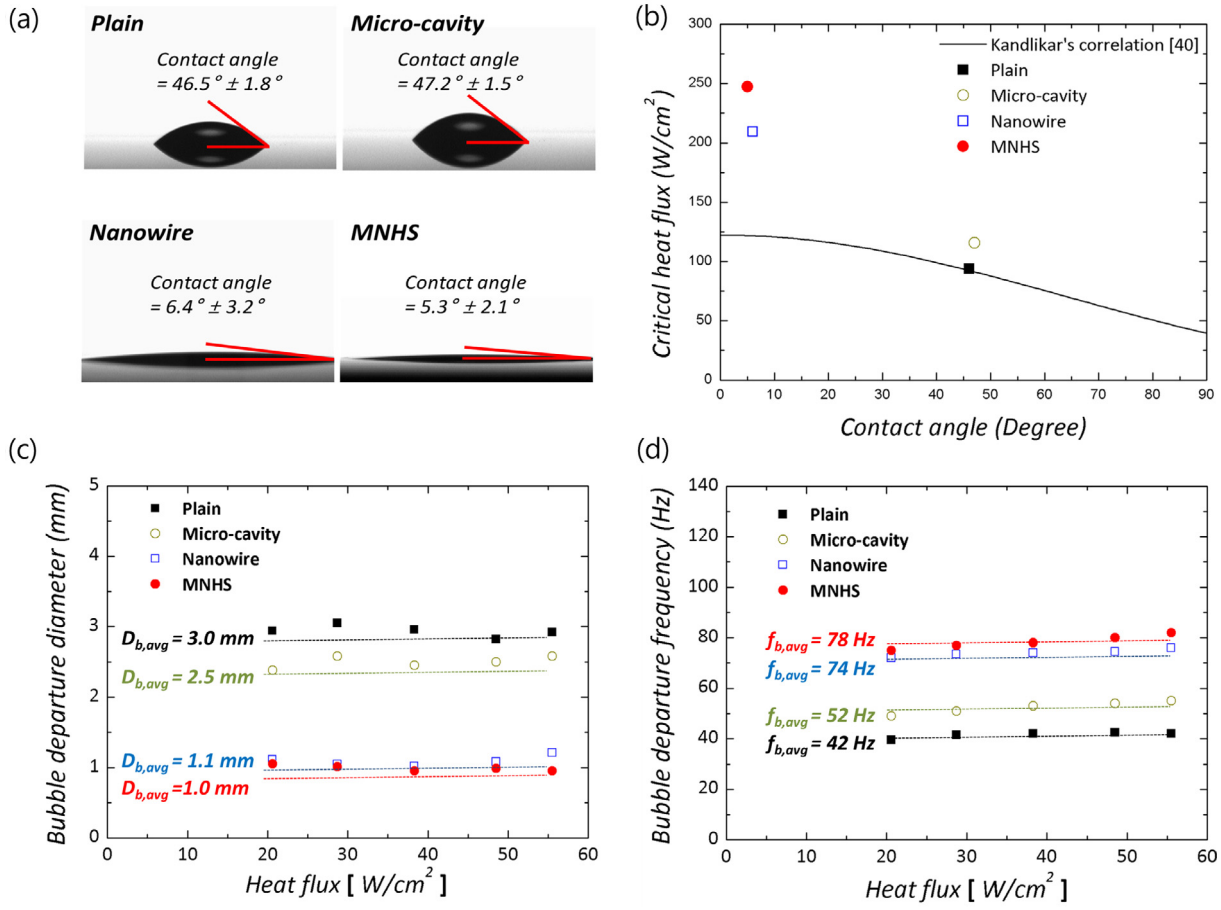

Fig. 5. (a) Apparent contact angles on various surfaces; plain, micro-cavity, nanowire and MNHS. (b) CHF for different contact angles comparison with theoretical correlation [40]. (c) Averaged bubble departure diameters and (d) bubble departure frequencies.

helping to increase the CHF (because bubble coalescence is delayed due to the decrease in bubble diameter and the increase in bubble departure frequency). From these results, MC has a role in reducing the bubble departure diameter and increasing the bubble frequency [41]. At the NW surface, CHF was enhanced by 121% compared with the plain surface. The reason for this is that surface wettability is increased due to the increase in surface roughness according to the Wenzel equation, as follows [42]:

$$\cos\theta = r \cdot \cos\theta^{*} \tag{3}$$

where θ is the apparent CA measured on the surface, r is a roughness factor and $\theta*$ is the equilibrium CA on an ideal plain surface. From the equation, the apparent CA decreases as the roughness increases. Additionally, the hemi-wicking phenomenon reported in previous works helps the water supply reach hot spots and enhances CHF compared with a plain surface [43]. Furthermore, NW has a positive effect on single bubble characteristics versus a plain surface and MC. NW has a 1/3 smaller diameter and a 3-fold higher frequency compared with the plain surface because NW has native cavities, of 1–2 μm, which confine and activate bubble departure at small diameters. As mentioned above, bubble diameter and frequency are related to delayed vapor film formation and the supply of water to the hot surface. Thus, we conclude that the enhanced CHF of the NW surface is due to positive effects of surface wettability and single bubble characteristics. However, this is not sufficient to explain the CHF enhancement of the MNHS, because the surface wettability, wicking behavior, and single bubble characteristics of the MNHS are almost the same as those of the NW surface. Thus, for a complete understanding of the CHF enhancement of MNHS, we should consider bubble merging to cause film boiling on the surface.

3.2. Bubble merging/departure characteristics and CHF enhancement

CHF is defined by a phenomenon whereby a vapor film covers the heating surface with violent bubble merging as heat flux increases [44]. Thus, a quantitative evaluation of bubble merging is important in demonstrating CHF. In the previous section, we evaluated the bubble's departure diameter, which indicates an independent bubble's equivalent diameter without any bubble merging. However, to understand CHF on the MNHS, we define the new concept of the merged bubble departure diameter instead. Fig. 6 shows the bubble coalescence phenomenon on a plain surface with time. When the bubbles nucleate on the surface, because bubble coalescence occurs on the heated surface in the lateral direction [45,46], small nucleated bubbles depart with a large merged bubble. From these results, the bubble merging phenomenon can be evaluated quantitatively by measuring the distribution of merged bubble departure diameter. As shown in Fig. 6, we evaluated how bubble coalescence occurred on the surface by measuring the distribution of merged bubble sizes. As shown in Fig. 7, merged bubble sizes were measured at three constant heat fluxes (28, 42, 55 W/cm^2), with 100 bubbles as the population. All surfaces showed a Gaussian distribution and the red dotted line in the graphs represents the averaged bubble departure diameter. The Gaussian function is as follows:

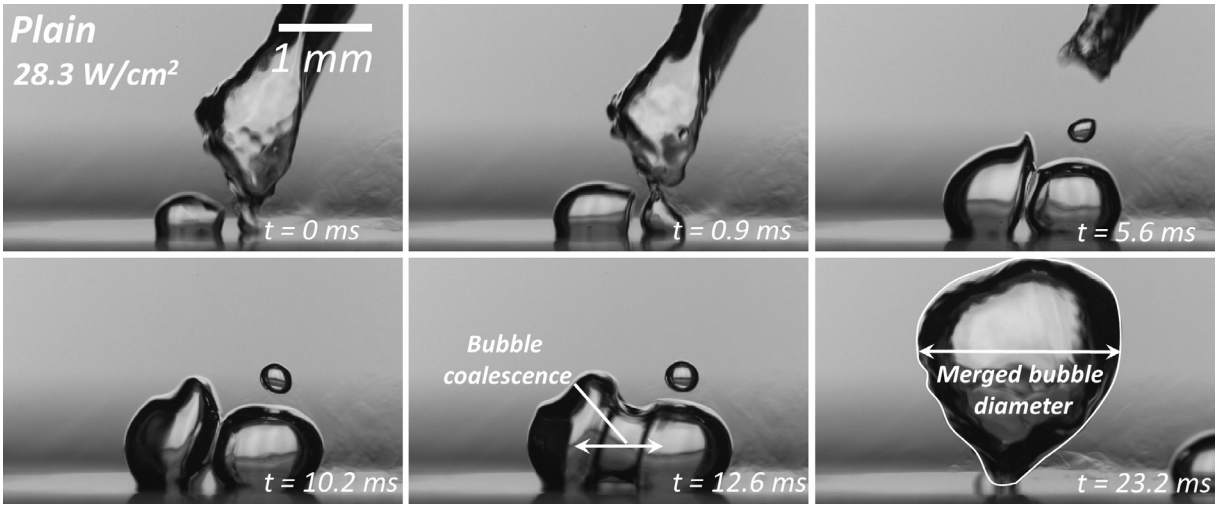

Fig. 6. Photographs of bubble coalescence characteristics at a heat flux of 28.3 W/cm^2 on the plain surface.

$$y = y_{0,cv} + \frac{A_{cv}}{w\sqrt{\pi/2}} e^{-2\frac{(x-x_{c,cv})^2}{w_{cv}^2}} \quad (4)$$

where $y_{0,cv}$, $x_{c,cv}$, w_{cv}, and A_{cv} indicate the off-set, center and width of the curve, and the area beneath the curve, respectively. A sharp shape of the Gaussian fit indicates that the variance is small, and a wide shape of the Gaussian fit means that the variance is large. By comparing the plain and MC surfaces in Fig. 7(a) and (b), the distances from the peak value of the merged diameter to the average bubble departure diameter at the three heat fluxes were shorter on the MC surface than on the plain surface. This means that bubble merging phenomena on the MC surface occurred less often than on the plain surface. Thus, we can predict that bubble merging is prevented by 'arranged' bubble nucleation, via the artificial micro cavities, on the MC surface. As shown in Fig. 7(c) and (d), the peak values of the merged diameters on MNHS at the three heat fluxes

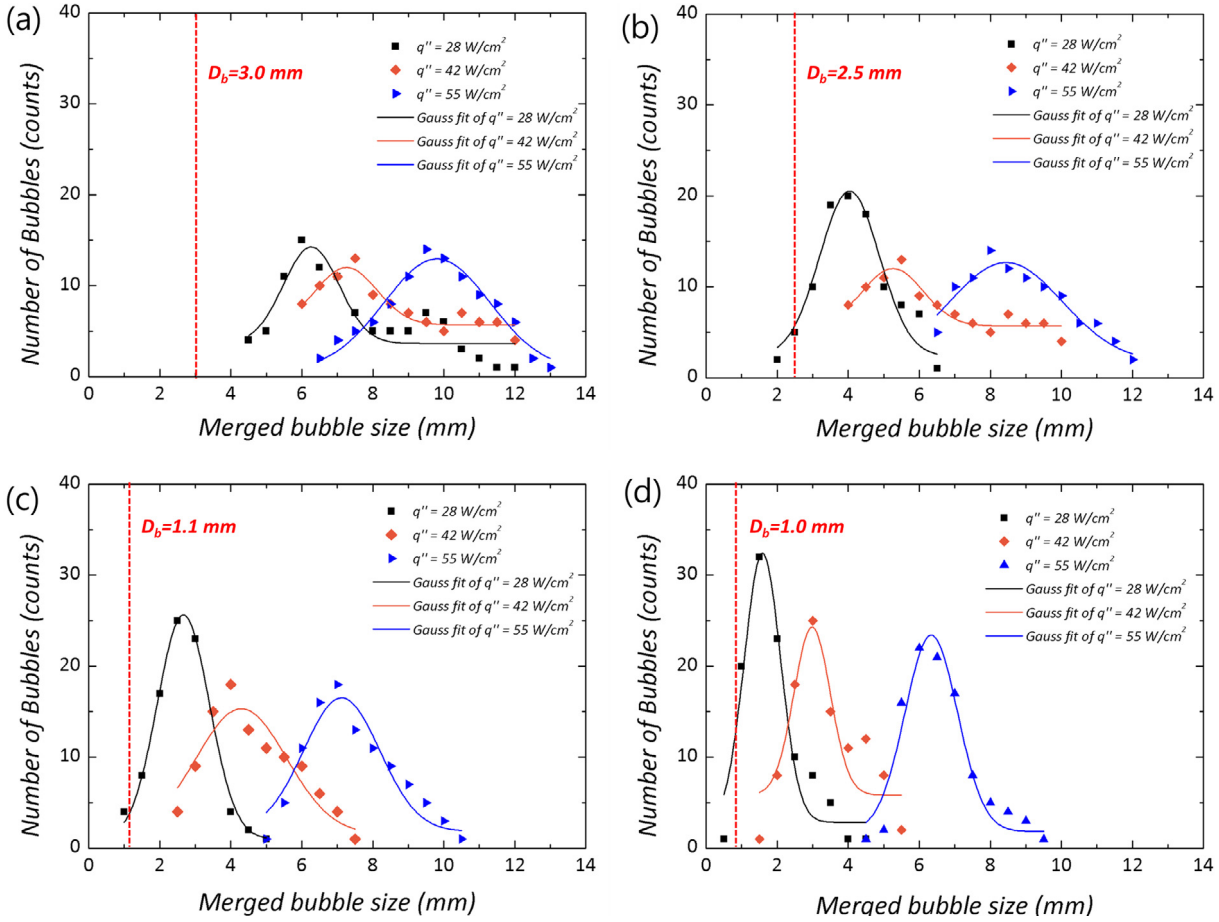

Fig. 7. Distributions of merged bubble sizes at heat flux q'' = 28 W/cm^2, 42 W/cm^2, 55 W/cm^2 of (a) plain, (b) micro-cavity, (c) nanowire and (d) MNHS. Inset values represent averaged single bubble departure diameter (D_b) on various surfaces; plain, micro-cavity, nanowire and MNHS.

were smaller than on the NW surface. This means that smaller, well-arranged bubbles are generated on the MNHS by the combined effect of bubble confinement from the natively formed micro cavities of the NW structure, and bubble arrangement as a result of the MC structures. In short, this means that arranged small bubbles are generated separately at nanowire-coated micro cavities of the MNHS, and bubble merging is delayed by the arranged MC structures and confined NW structures. Fig. 8(a) and (b) shows averaged values and standard deviations of merged bubble diameters on the four surfaces as the heat flux increases. As shown in Fig. 8 (a) and (b), the MNHS's average value and standard deviation of merged bubble size at high heat flux (55 W/cm^2) decreased to less than 65% and 28%, respectively, compared to that of the plain surface. This means that bubble merging phenomena are minimized on MNHS, due to its arranged confined bubble generation by the arrangement of MC structures and the confined NW structures. Thus, the CHF of the MNHS can be maximized by delaying bubble merging and retaining a liquid path to supply coolant to the surface of the MNHS better than on the NW surface.

Fig. 9(a) shows CHF on plain, MC, and NW surfaces, and on MNHS. As mentioned above, the MC surface showed slightly smaller and faster bubble nucleation compared with the plain surface, by confining the bubble growth size because of the arrangement of micro cavities. Thus, CHF was enhanced by 24% on the MC surface, by delaying bubble merging. The NW surface generates significantly numerous smaller and faster bubbles compared with the plain surface, by means of numerous 1–2 μm natively formed micro-cavities. Thus, by combining effect of the large bubble density and superhydrophilic characteristics of the NW morphology, CHF is enhanced by 121% compared with the plain surface. Because MNHS combines the effects of NW and MC surfaces, it showed the largest CHF (172% increase compared with a plain surface). This effect also can be explained by the normalized pitch of the nucleation sites (S_{avg}/D_{avg}), which indicates a relationship between the averaged bubble departure size and the pitch of the nucleation sites, as shown in Fig. 9(b). On the plain surface, when the pitch of the nucleation sites is larger than the bubble departure diameter, because it cannot retain enough bubble density compared to other 3 surfaces, it records the smallest CHF by 94.8 W/cm^2. When the pitch of the nucleation sites is smaller than the bubble departure diameter on the MC surface, although it secured larger bubble density compared to plain surface, because it is easy to merge the nucleated bubbles, CHF increases by only 24% compared with the plain surface. NW surface ensures much larger bubble density compared to MC surface by means of numerous 1–2 μm natively formed micro cavities, CHF is increased by 118% compared to plain surface. However, because NW surface has smaller pitch of the nucleation sites than the bubble departure diameter similar to MC surface, it has limitation for enhancing CHF due to easiness of bubble coalescence. When the pitch of the nucleation sites is about the same as the bubble departure diameter on MNHS, CHF is increased remarkably, by 172%, versus the plain surface. In other words, when the normalized pitch of the nucleation sites was 1, namely the pitch of the nucleation sites and the bubble nucleation size had the same dimension, CHF can be maximized by delaying bubble coalescence and maximizing bubble density. Thus, through optimization of bubble nucleation sites for 'arranged' bubble departure from the surface, CHF enhancement can be achieved for boiling heat transfer.

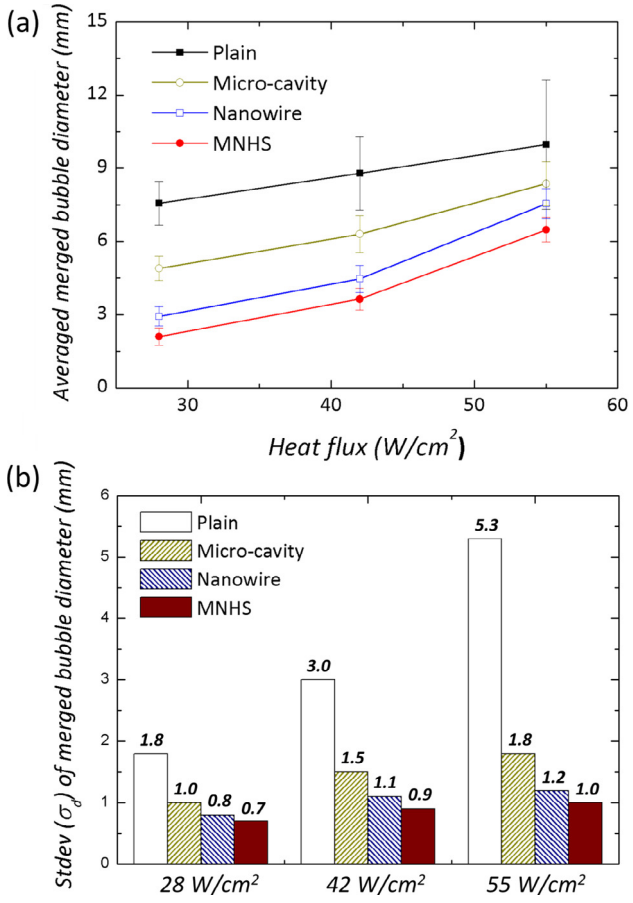

Fig. 8. (a) Averaged merged bubble diameters and (b) Standard deviations of merged bubble diameters for various surfaces; plain, micro-cavity, nanowire and MNHS.

3.3. Enhancement of spatial and temporal temperature uniformity

The thermal uniformity and stability of a boiling surface are the most important factors in long-term boiling application, because boiling surface failure with local hot spots can be avoided by keeping the overall spatial/temporal surface temperature uniformity [33,34,47–50]. Fig. 10(a) and (b) shows spatial temperature uniformity at heat fluxes of 22 W/cm^2 (low heat flux) and CHF on plain, MC, and NW surfaces, and on MNHS. As shown in the inset of Fig. 10(a), the temperatures at the five RTD sensors represent the spatial surface temperature distribution with heat flux, and the

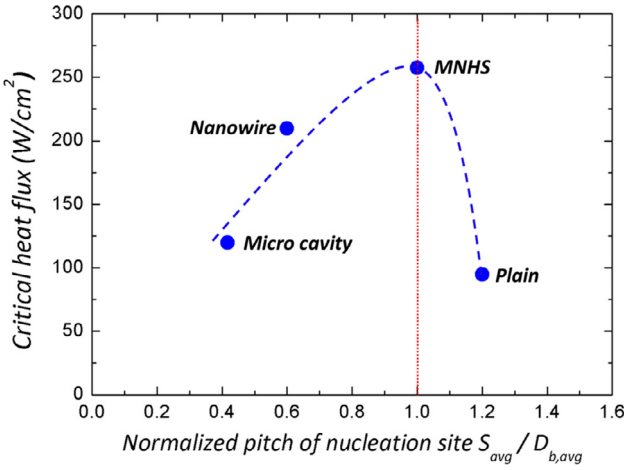

Fig. 9. CHF for variation of normalized pitch of nucleation sites (red dotted line of $S_{avg}/D_{b,avg}$ = 1 means that the pitch of the nucleation sites and the bubble departure size have the same dimension). (For interpretation of the references to color in this figure legend, the reader is referred to the web version of this article.)

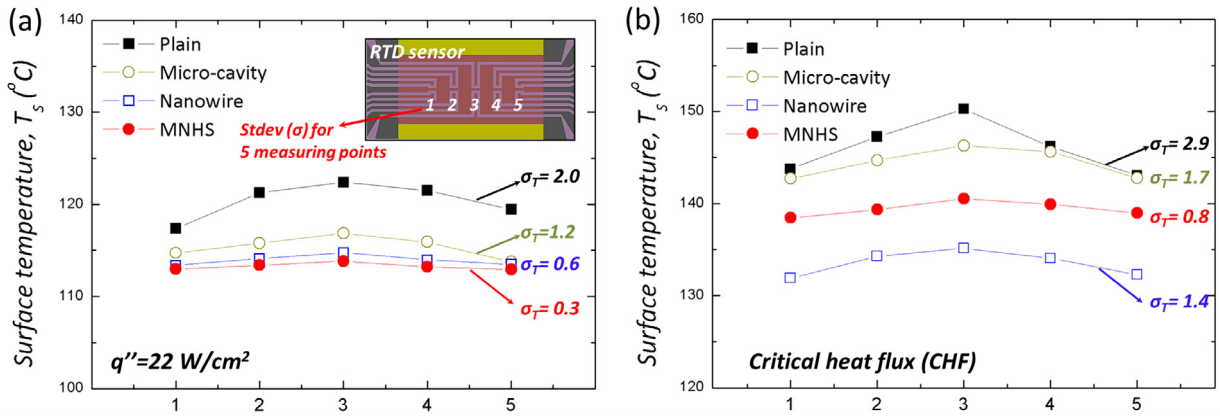

Fig. 10. Spatial temperature distributions for different RTD sensor locations 1–5 at (a) 22 W/cm^2 and (b) CHF on various surfaces; plain, micro-cavity, nanowire and MNHS.

inset numbers are the standard deviations of the spatial temperatures at the five RTD sensors. As shown in Fig. 10(a), at the low heat flux (22 W/cm^2), the standard deviations of spatial temperatures were 2.0 K, 1.2 K, and 0.6 K on the plain, MC, and NW surfaces, respectively. MNHS showed the smallest standard deviation, of 0.3 K. In Fig. 10(b), this outstanding spatial temperature uniformity was also maintained on MNHS surface at CHF. As shown in Fig. 10 (b), at CHF, the standard deviations of spatial temperatures were 2.9 K, 1.7 K, and 1.4 K on the plain, MC, and NW surfaces, respectively. In fact, the standard deviation of the temperatures was only 0.8 on the MNHS surface at CHF. The reason for this is that small, fast, and well-arranged bubbles are generated not only by the natively formed micro cavities of the NW structure for small nucleation, but also the arranged micro cavities of MC structure for arranged nucleation. Fig. 11(a), (b), (c) and (d) shows the temporal temperature uniformity with time on the plain, MC, and NW surfaces and MNHS, respectively. As shown in the inset of Fig. 11(a), temporal uniformity is indicated by temperature variation with time on RTD sensor location 3, and the inset red number shows the standard deviation of temperature variation with time. The standard deviation of temperature variation with time decreased, to 1.8 K and 1.0 K at CHF on the MC and NW surfaces, respectively. Similarly, the MNHS surface showed the lowest standard deviation, of 0.6 K at CHF.

In summary, the MNHS can generate small, fast, and dispersed bubbles because of the confining effects of the NW structures

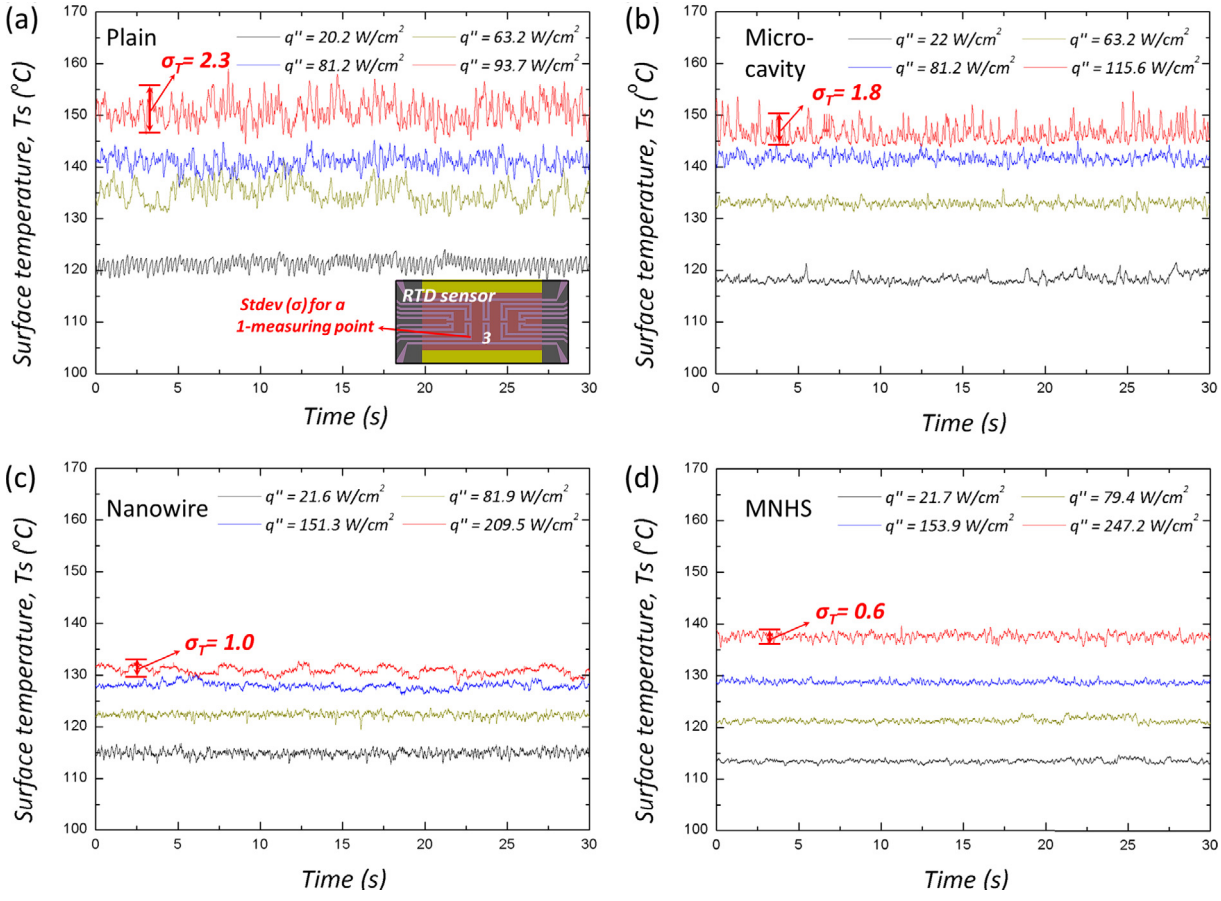

Fig. 11. Temporal temperature variation at RTD sensor location 3 for different heat fluxes on various surfaces; (a) plain, (b) micro-cavity, (c) nanowire and (d) MNHS.

and the arranged nucleation effect of the MC structures. Consequently, because the bubble nucleation region and liquid supply region are separated on the MNHS, bubble merging is delayed significantly. Additionally, this allows a large spatial and temporal vacant area between the bubbles to contact with the boiling surface and working fluid directly. In conclusion, CHF is increased markedly on the MNHS versus the NW surface. Moreover, the small, fast, and arranged dispersed bubbles generated on the MNHS enable long-term thermal uniformity and stability, as evidenced by the standard deviations of spatial/temporal temperature variation at CHF, reduced to less than 1/3 and 1/4, respectively, compared with the plain surface. In conclusion, we demonstrated the possibility of using the MNHS for enhancing not only CHF, but also thermal uniformity/stability in long-term boiling applications.

4. Conclusion

In this study, the advantages of an MNHS are discussed for enhancing thermal uniformity/stability and boiling heat transfer performance. Spatial/temporal heat transfer characteristics were evaluated on MNHS using a local temperature-measuring sensor of resistance temperature detector (RTD). We demonstrated that MNHS could enhance thermal uniformity/stability by the confining effects of nucleated bubble on NW structures, and uniform bubble nucleation on uniformly distributed MC structures. By these combined effects of the NW and MC structures, which can delay the bubble coalescence phenomenon, MNHS also enhanced CHF by catalyzing bubble nucleation dispersedly and quickly at small sizes. As a result, boiling heat transfer using MNHS shows a breakthrough, reducing the spatial and temporal temperature variation at high heat flux region or CHF to less than 1/3 and 1/4, respectively, compared with a plain surface. When the normalized pitch of nucleation sites is 1, that is, the pitch of the nucleation sites equal to the bubble size, CHF is enhanced markedly (>170%) on MNHS versus a plain surface, by delaying bubble coalescence and maximizing the bubble density. Thus, the ratio of the average pitch of nucleation sites to bubble departure size, which affects the probability of bubble coalescence, can be an important factor for CHF improvement when designing an MNHS. Further study, the aligned nanowires or micro-pillars which have outstanding wicking performance can be applied on MNHS for further enhancement of CHF [51,52]. These demonstrations and results will be applicable to thermal and fluidic designs of micro-device cooling, as well as macro-system cooling, in applications ranging from electrical device cooling to power-plant system cooling under harsh thermal conditions.

Acknowledgement

This work was supported by the Center for Advanced MetaMaterials (CAMM) funded by the Ministry of Science, ICT and Future Planning as Global Frontier Project (CAMM-No. NRF-2014M3A6B3063716) and the Human Resources Development program (No. 20174030201720) of the Korea Institute of Energy Technology Evaluation and Planning (KETEP), grant funded by the Korea government Ministry of Trade, Industry and Energy.

Appendix A. Supplementary material

Supplementary data associated with this article can be found, in the online version, at https://doi.org/10.1016/j.applthermaleng.2017.10.144.

References

[1] C.-H. Choi, M. David, Z. Gao, A. Chang, M. Allen, H. Wang, et al., Large-scale generation of patterned bubble arrays on printed Bi-functional boiling surfaces, Sci. Rep. 6 (2016).
[2] S. You, T.W. Simon, A. Bar-Cohen, A technique for enhancing boiling heat transfer with application to cooling of electronic equipment, IEEE Trans. Compon. Hybr. 15 (1992) 823–831.
[3] Z. Wu, B. Sundén, On further enhancement of single-phase and flow boiling heat transfer in micro/minichannels, Renew. Sust. Energy Rev. 40 (2014) 11–27.
[4] S. Gong, P. Cheng, Direct numerical simulations of pool boiling curves including heater's thermal responses and the effect of vapor phase's thermal conductivity, Int. Commun. Heat Mass Transf. 87 (2017) 61–71.
[5] V.P. Carey, Liquid-Vapor Phase Change Phenomena, Taylor & Francis, 1992.
[6] H. O'Hanley, C. Coyle, J. Buongiorno, T. McKrell, L.-W. Hu, M. Rubner, et al., Separate effects of surface roughness, wettability, and porosity on the boiling critical heat flux, Appl. Phys. Lett. 103 (2013) 024102.
[7] K.-H. Chu, R. Enright, E.N. Wang, Structured surfaces for enhanced pool boiling heat transfer, Appl. Phys. Lett. 100 (2012) 241603.
[8] A. Ustinov, V. Ustinov, J. Mitrovic, Pool boiling heat transfer of tandem tubes provided with the novel microstructures, Int. J. Heat Fluid Flow 32 (2011) 777–784.
[9] S.H. Kim, G.C. Lee, J.Y. Kang, K. Moriyama, M.H. Kim, H.S. Park, Boiling heat transfer and critical heat flux evaluation of the pool boiling on micro structured surface, Int. J. Heat Mass Transf. 91 (2015) 1140–1147.
[10] H. Honda, H. Takamastu, J. Wei, Enhanced boiling of FC-72 on silicon chips with micro-pin-fins and submicron-scale roughness, J. Heat transf. 124 (2002) 383–390.
[11] J.J. Wei, H. Honda, Effects of fin geometry on boiling heat transfer from silicon chips with micro-pin-fins immersed in FC-72, Int. J. Heat Mass Transf. 46 (2003) 4059–4070.
[12] D. Guo, J.J. Wei, Y.H. Zhang, Enhanced flow boiling heat transfer with jet impingement on micro-pin-finned surfaces, Appl. Therm. Eng. 31 (2011) 2042–2051.
[13] A. Suszko, M.S. El-Genk, Bubbles transient growth in saturation boiling of PF-5060 dielectric liquid on dimpled Cu surfaces, J. Therm. Sci. Eng. Appl. 8 (2016) 021016.
[14] J. O'Connor, S. You, J. Chang, Gas-saturated pool boiling heat transfer from smooth and microporous surfaces in FC-72, J. Heat Transf. 118 (1996) 662–667.
[15] D.E. Kim, D.I. Yu, S.C. Park, H.J. Kwak, H.S. Ahn, Critical heat flux triggering mechanism on micro-structured surfaces: Coalesced bubble departure frequency and liquid furnishing capability, Int. J. Heat Mass Transf. 91 (2015) 1237–1247.
[16] Y. Im, C. Dietz, S.S. Lee, Y. Joshi, Flower-like CuO nanostructures for enhanced boiling, Nanoscale Microscale Thermophys. Eng. 16 (2012) 145–153.
[17] S. Shin, T.T. Al-Housseiny, B.S. Kim, H.H. Cho, H.A. Stone, The race of nanowires: morphological instabilities and a control strategy, Nano Lett. 14 (2014) 4395–4399.
[18] E. Demir, T. Izci, A.S. Alagoz, T. Karabacak, A. Koşar, Effect of silicon nanorod length on horizontal nanostructured plates in pool boiling heat transfer with water, Int. J. Therm. Sci. 82 (2014) 111–121.
[19] Y. Tang, B. Tang, Q. Li, J. Qing, L. Lu, K. Chen, Pool-boiling enhancement by novel metallic nanoporous surface, Exp. Therm. Fluid Sci. 44 (2013) 194–198.
[20] B. Shi, Y.-B. Wang, K. Chen, Pool boiling heat transfer enhancement with copper nanowire arrays, Appl. Therm. Eng. 75 (2015) 115–121.
[21] R. Chen, M.C. Lu, V. Srinivasan, Z. Wang, H.H. Cho, A. Majumdar, Nanowires for enhanced boiling heat transfer, Nano Lett. 9 (2009) 548–553.
[22] S. Shin, G. Choi, B.S. Kim, H.H. Cho, Flow boiling heat transfer on nanowire-coated surfaces with highly wetting liquid, Energy 76 (2014) 428–435.
[23] C. Li, Z. Wang, P.I. Wang, Y. Peles, N. Koratkar, G.P. Peterson, Nanostructured copper interfaces for enhanced boiling, Small 4 (2008) 1084–1088.
[24] H. Jo, S. Kim, H. Kim, J. Kim, M.H. Kim, Nucleate boiling performance on nano/microstructures with different wetting surfaces, Nanoscale Res. Lett. 7 (2012) 242.
[25] D.E. Kim, D.I. Yu, D.W. Jerng, M.H. Kim, H.S. Ahn, Review of boiling heat transfer enhancement on micro/nanostructured surfaces, Exp. Therm. Fluid Sci. 66 (2015) 173–196.
[26] H.S. Ahn, C. Lee, J. Kim, M.H. Kim, The effect of capillary wicking action of micro/nano structures on pool boiling critical heat flux, Int. J. Heat Mass Transf. 55 (2012) 89–92.
[27] Z. Yao, Y.-W. Lu, S.G. Kandlikar, Fabrication of nanowires on orthogonal surfaces of microchannels and their effect on pool boiling, J. Micromech. Microeng. 22 (2012) 115005.
[28] S. Kim, H.D. Kim, H. Kim, H.S. Ahn, H. Jo, J. Kim, M.H. Kim, Effects of nano-fluid and surfaces with nano structure on the increase of CHF, Exp. Therm. Fluid Sci 34 (4) (2010) 487–495.
[29] S. Shin, B.S. Kim, G. Choi, H. Lee, H.H. Cho, Double-templated electrodeposition: simple fabrication of micro-nano hybrid structure by electrodeposition for efficient boiling heat transfer, Appl. Phys. Lett. 101 (2012) 251909.
[30] M.M. Rahman, J. Pollack, M. McCarthy, Increasing boiling heat transfer using low conductivity materials, Sci. Rep. 5 (2015).

[31] B.S. Kim, S. Shin, S.J. Shin, K.M. Kim, H.H. Cho, Micro-nano hybrid structures with manipulated wettability using a two-step silicon etching on a large area, Nanoscale Res. Lett. 6 (2011) 1–10.
[32] B.S. Kim, S. Shin, D. Lee, G. Choi, H. Lee, K.M. Kim, et al., Stable and uniform heat dissipation by nucleate-catalytic nanowires for boiling heat transfer, Int. J. Heat Mass Transf. 70 (2014) 23–32.
[33] P. Koch, Equivalent diameters of rectangular and oval ducts, Build Serv. Eng. Res. Technol. 29 (2008) 341–347.
[34] B.S. Kim, G.M. Yang, S. Shin, G. Choi, H.H. Cho, Local nucleation propagation on heat transfer uniformity during subcooled convective boiling, Heat Mass Transf. 51 (2015) 1–9.
[35] R.J. Moffat, Describing the uncertainties in experimental results, Exp. Therm. Fluid Sci. 1 (1988) 3–17.
[36] H. Jo, D.I. Yu, H. Noh, H.S. Park, M.H. Kim, Boiling on spatially controlled heterogeneous surfaces: wettability patterns on microstructures, Appl. Phys. Lett. 106 (2015) 181602.
[37] D.E. Kim, S.C. Park, D.I. Yu, M.H. Kim, H.S. Ahn, Enhanced critical heat flux by capillary driven liquid flow on the well-designed surface, Appl. Phys. Lett. 107 (2015) 023903.
[38] M. Zhang, K. Lian, Using bulk micromachined structures to enhance pool boiling heat transfer, Microsyst. Technol. 14 (2008) 1499–1505.
[39] N. Basu, G.R. Warrier, V.K. Dhir, Onset of nucleate boiling and active nucleation site density during subcooled flow boiling, J. Heat Transf. 124 (2002) 717.
[40] S.G. Kandlikar, A theoretical model to predict pool boiling CHF incorporating effects of contact angle and orientation, J. Heat Transf. 123 (2001) 1071–1079.
[41] L. Dong, X. Quan, P. Cheng, An experimental investigation of enhanced pool boiling heat transfer from surfaces with micro/nano-structures, Int. J. Heat Mass Transf. 71 (2014) 189–196.
[42] B.S. Kim, S. Shin, S.J. Shin, K.M. Kim, H.H. Cho, Control of superhydrophilicity/superhydrophobicity using silicon nanowires via electroless etching method and fluorine carbon coatings, Langmuir 27 (2011) 10148–10156.
[43] B.S. Kim, H. Lee, S. Shin, G. Choi, H.H. Cho, Interfacial wicking dynamics and its impact on critical heat flux of boiling heat transfer, Appl. Phys. Lett. 105 (2014) 191601.
[44] J. Kim, Review of nucleate pool boiling bubble heat transfer mechanisms, Int. J. Multiph. Flow 35 (2009) 1067–1076.
[45] J. Bonjour, M. Clausse, M. Lallemand, Experimental study of the coalescence phenomenon during nucleate pool boiling, Exp. Therm. Fluid Sci. 20 (2000) 180–187.
[46] L. Zhang, M. Shoji, Nucleation site interaction in pool boiling on the artificial surface, Int. J. Heat Mass Transf. 46 (2003) 513–522.
[47] N.S. Dhillon, J. Buongiorno, K.K. Varanasi, Critical heat flux maxima during boiling crisis on textured surfaces, Nat. Commun. 6 (2015).
[48] S. Zhang, Y. Tang, J. Zeng, W. Yuan, J. Chen, C. Chen, Pool boiling heat transfer enhancement by porous interconnected microchannel nets at different liquid subcooling, Appl. Therm. Eng. 93 (2016) 1135–1144.
[49] M. Dharmendra, S. Suresh, C.S. Sujith Kumar, Q. Yang, Pool boiling heat transfer enhancement using vertically aligned carbon nanotube coatings on a copper substrate, Appl. Therm. Eng. 99 (2016) 61–71.
[50] B. Li, X. Han, Z. Wan, X. Wang, Y. Tang, Influence of ultrasound on heat transfer of copper tubes with different surface characteristics in sub-cooled boiling, Appl. Therm. Eng. 92 (2016) 93–103.
[51] D.I. Shim, G. Choi, N. Lee, T. Kim, B.S. Kim, H.H. Cho, Enhancement of pool boiling heat transfer using aligned silicon nanowires array, ACS Appl. Mater. Interf. 9 (2017) 17595.
[52] J. Li, Y. Hou, Y. Liu, C. Hao, M. Li, M.K. Chaudhury, et al., Directional transport of high-temperature Janus droplets mediated by structural topography, Nat. Phys. 12 (2016) 606–612.